

Particle-resolved simulation of freely evolving particle suspensions: Flow physics and modeling

Vahid Tavanashad^{a,b}, Alberto Passalacqua^{a,b}, Shankar Subramaniam^{a,b,*}

^a*Department of Mechanical Engineering, Iowa State University, Ames, IA 50011, USA*

^b*Center for Multiphase Flow Research & Education (CoMFRE), Iowa State University, Ames, IA 50011, USA*

Abstract

The objective of this study is to understand the dynamics of freely evolving particle suspensions over a wide range of particle-to-fluid density ratios. The dynamics of particle suspensions are characterized by the average momentum equation, where the dominant contribution to the average momentum transfer between particles and fluid is the average drag force. In this study, the average drag force is quantified using particle-resolved direct numerical simulation in a canonical problem: a statistically homogeneous suspension where an imposed mean pressure gradient establishes a steady mean slip velocity between the phases. The effects of particle velocity fluctuations, particle clustering, and mobility of particles are studied separately. It is shown that the competing effects of these factors could decrease, increase, or keep constant the drag of freely evolving suspensions in comparison to fixed beds at different flow conditions. It is also shown that the effects of particle clustering and particle velocity fluctuations are not independent. Finally, a correlation for interphase drag force in terms of volume fraction, Reynolds number, and density ratio is proposed. Two different approaches (symbolic regression and predefined functional forms)

*This is a post-peer-review, pre-copyedit version of an article published in International Journal of Multiphase Flow. The final authenticated version is available online at: <https://doi.org/10.1016/j.ijmultiphaseflow.2020.103533>.

©2020. This manuscript version is made available under the CC-BY-NC-ND 4.0 license <http://creativecommons.org/licenses/by-nc-nd/4.0/>.

*Corresponding author

Email address: shankar@iastate.edu (Shankar Subramaniam)

October 29, 2021

are used to develop the drag correlation. Since this drag correlation has been inferred from simulations of particle suspensions, it includes the effect of the motion of the particles. This drag correlation can be used in computational fluid dynamics simulations of particle-laden flows that solve the average two-fluid equations where the accuracy of the drag law affects the prediction of overall flow behavior.

Keywords: Particle clustering, Particle velocity fluctuations, Particle mobility, Particle-resolved direct numerical simulation, Drag law, Particle-laden flows

1. Introduction

Dispersed multiphase flows are encountered when one phase in the form of bubbles, droplets, or particles is dispersed within a fluid called the carrier phase, and they include gas–solid, solid–liquid, and gas–liquid flows. Such flows are common in both nature (e.g., solid particles or rain droplets in the air) and industry (e.g., bubble columns and fluidized bed reactors). Understanding momentum and kinetic energy exchange between dispersed and carrier phases is central to predicting the behavior of many multiphase flows. Although we can use both experimental and numerical studies to explore the interaction between carrier and dispersed phases, particle-resolved direct numerical simulation (PR-DNS) has proven to be a useful tool for understanding flow physics and model development [1, 2]. However, PR-DNS of industrial multiphase processes in realistic geometries at scale is not feasible, even on today’s supercomputers, due to its computational cost.

On the other hand, multiphase computational fluid dynamics (CFD) simulations that solve the averaged equations of multiphase flow are increasingly being used as an efficient alternative for design optimization because experiments are often costly and time-consuming. CFD simulations of multiphase flow are based on either the Eulerian–Lagrangian (EL) or the Eulerian–Eulerian (EE) two-fluid approach. In the EE method, each phase is treated as a continuous medium interpenetrating the other phase and is represented by macroscopic conservation

equations, which are valid throughout the entire flow domain. The averaging process results in unclosed terms that represent interphase interactions and need to be modeled. For instance, the mean momentum conservation equation in the particle phase requires closure of the mean drag force. This closure for the mean drag force is popularly known as a *drag law* and is typically obtained from a combination of theoretical, experimental, and computational studies.

In the EL approach, the trajectory of each particle is tracked in response to collisional and hydrodynamic forces, while the carrier flow is represented in a Eulerian frame. The particles can be considered *point particles* if their diameter is smaller than the smallest scales of fluid motion and in this case, we can use a grid size larger than the size of the particles which means the flow field on the particle surface is not resolved. The majority of EL simulations to date have been using the point-particle approach. However, in recent years, EL methods are being extended to finite-size particles, whose diameter is comparable to the mesh spacing, using volume-filtering [3]. In the case of finite-size EL methods, there are still outstanding questions as to how to couple the dispersed and carrier phases [4]. Therefore, the interaction between particles and the surrounding flow, which is typically referred to as the drag correlation must be modeled using empirical relations or PR-DNS.

An accurate drag correlation for the representation of the average inter-phase momentum transfer term is essential to perform predictive CFD simulations. However, it should be mentioned that there are different averaging approaches for EE methods including time-averaging [5], volume-averaging [6, 7], ensemble-averaging [8–10]. The volume-averaging approach by Anderson and Jackson [6] also involved filtering the fluid and particle fields. Capecelatro and Desjardins [3] extended this filtering approach to EL method and developed the volume-filtered Euler-Lagrange (VFEL) method.

Although these averaging methods look similar, they are fundamentally different, and there has been a discussion on their validity and connection in the literature [11]. Recently, Subramaniam [12] showed the differences between the volume-averaging and ensemble-averaging, employing a simple example based

on the mass conservation equation. Consistency of the PR-DNS and EE approaches requires that the method used to calculate the surface force density in the PR-DNS should be consistent with the definition of the average interphase momentum transfer term. Otherwise, the drag correlation inferred from PR-DNS may not be consistent with the EE equations that arise from the two-fluid theory [13]. A detailed discussion on the connection of PR-DNS equations and ensemble-averaged two-fluid equations is presented by [13].

Several researchers have studied the interphase momentum transfer (drag exchange) between phases in particle-laden flows. This is usually done in an idealized canonical flow problem in which the dispersed phase consists of monodisperse spherical objects which are fixed and distributed homogeneously in a periodic domain. Fixed beds are a good approximation for gas–solid flows with high inertia particles. This special case is well-studied and several drag correlations are proposed in the literature [13–22]. These studies have also been extended to bidisperse particles [16, 17, 23–25] as well as clustered [26] or inhomogeneous [27, 28] configuration of particles.

As an improvement of fixed bed simulations, simulating stationary particles with an assigned non-zero velocity has been performed to investigate the effect of fluctuating particle acceleration on particle velocity fluctuations [29] and the effects of particle velocity fluctuations on interphase drag [30–32] and heat transfer [33] in gas–solid flows.

Particle-resolved simulations of freely evolving suspensions of gas–solid and solid–liquid flows [28, 29, 34–39] have also been performed in the past years with a focus on studying the interphase drag force. Although the effects of particle velocity fluctuations, clustering, or mobility on mean drag have been investigated in these studies, none of them present a complete description of the effects of these three factors. These works only explain the change of drag compared to fixed beds by considering one factor at a time. The only exception is the work by Rubinstein et al. [38], who consider both particle mobility and clustering but only for low-Reynolds number flows.

Most recently, Tavanashad and Subramaniam [40] proposed a PR-DNS-

based drag law for buoyant particle suspensions which are a good approximation to spherical bubbles in contaminated liquid [41–43]. They showed that with proper scaling, the drag of buoyant particles is comparable with the drag of bubbles in clean liquid [44, 45].

In this work, we have performed PR-DNS for a wide range of density ratio to cover both heavy and light particles. Then we have studied the effects of the factors mentioned above (particle clustering, particle velocity fluctuations, and particle mobility) separately and also altogether in particle-laden flows. Finally, an improved drag correlation is proposed, which can be used for calculating the drag force in EE and EL simulations of particles with different densities. In developing our correlation, we have used two different approaches: symbolic regression and a predefined functional form. We have also discussed which variables the drag correlation should depend on to account for particle motion. In the following, we have summarized the discussion on the effects of particle clustering, particle velocity fluctuations, and mobility of particles on the mean drag in dispersed multiphase flows from the literature.

Particle clustering: The emergence of clustering in the simulation of freely evolving suspensions of solid particles or bubbles has already been reported in the literature. Prior works have shown that nearly spherical bubbles form clusters and generate horizontal planes of bubbles, known as rafts, perpendicular to the flow direction in bubbly flows, which increases the drag force [45–48]. Yin and Koch [48] compared the microstructure of particle and bubble suspensions at intermediate Reynolds numbers ($Re = 5.4, 20$) and volume fractions ($\phi < 0.25$) and showed that horizontal clustering occurs in both systems but it is more significant for bubble suspensions. On the other hand, vertically elongated columnar particle clusters are observed in dilute systems at high Reynolds number in gas–solid flows, which reduce the average drag force [39, 49]. Moreover, Wang et al. [27] and Zhou et al. [28] have found from the simulation of an inhomogeneous fixed bed that the drag force depends on both the direction and magnitude of the particle volume fraction gradient, with volume fraction gradients in the direction of the mean slip velocity causing an increase in drag,

and volume fraction gradients perpendicular to the slip velocity causing a decrease in drag. It is also known that isotropic clustering in the fixed assembly of particles always decreases the drag [26, 27]. The importance of considering the particle structure in modeling drag has also been the topic of a recent review paper by Sundaresan et al. [50].

Particle velocity fluctuations: The mean relative motion of particles/bubbles is responsible for the generation of fluid velocity fluctuations, which in turn modify velocity fluctuations in particles/bubbles and the mean relative motion (or drag force) between phases [51, 52]. In prior works, it is shown that particle velocity fluctuations act as a source for an increase in the drag of gas–solid flows [29, 30, 36, 53]. Most recently, Tavanashad et al. [54] studied particle suspensions for a wide range of density ratio ($0.001 \leq \rho_p/\rho_f \leq 1000$) at Reynolds number 20. They showed that for this Reynolds number, drag does not change significantly with density ratio even though particle and fluid velocity fluctuations increase with decreasing density ratio. The present work extends the range of that study and examines whether this trend persists at all Reynolds number in the range 10 to 100.

Particle Mobility: The ability of the particles to translate and rotate due to the effects of the surrounding fluid can decrease the drag on particles [37]. In fact, light particles follow the streamlines of fluid, and for heavier ones, they continue moving on their initial trajectory.

2. Numerical method

The PR-DNS approach used in this work is based on the discrete-time direct forcing immersed boundary method of Mohd-Yusof [55] and is called the particle-resolved uncontaminated-fluid reconcilable immersed boundary method (PUReIBM). The PUReIBM methodology is explained in detail and validated for simulating fixed beds [13, 56], gas–solid flows [29, 57, 58], and buoyant particles [40]. Here, the main features of this method are presented.

In PUReIBM, the continuity and the Navier–Stokes equations are solved for

the fluid phase on a uniform Cartesian grid with the Crank–Nicolson scheme for the viscous terms and an Adams–Bashforth scheme for the convective terms. The boundary conditions on the fluid velocity at the particle interface (no-slip and no-penetration) are imposed via a source term (immersed boundary force) in the Navier-Stokes equations.

The motion of each particle in PUREIBM is evolved by updating its position and translational and rotational velocities, according to Newton’s second law. A soft-sphere collision [59] model is used to capture particle-particle interactions. Particles are allowed to overlap during a collision, and the contact mechanics between the overlapping particles are modeled by a spring in the normal direction (elastic collisions). The spring causes the colliding particles to rebound. The particles are assumed to be frictionless during collisions. This implies that the tangential component of the contact force is zero.

To stabilize the simulations for buoyant particles, the virtual force stabilization technique introduced by Schwarz et al. [60] is utilized, which is extended for simulation of dense suspensions [40]. The simulation of buoyant particles in this work can also be considered as an approximation to bubbly flows when the presence of surfactants contaminates the surrounding fluid, and the no-slip velocity boundary condition is valid at the interface of bubbles [41–43].

3. Simulation setup

In this study, simulations are performed in a cubic domain with periodic boundary conditions. A constant mean pressure gradient is imposed in the x -direction that accelerates the particles and the fluid. Both the mean fluid velocity and the mean particle velocity increase; however, their difference—the mean slip velocity—reaches a statistically stationary state. The magnitude of the mean pressure gradient depends on three parameters: the dispersed phase volume fraction ϕ , the particle-to-fluid density ratio ρ_p/ρ_f , and a Reynolds number defined as:

$$Re_m = \frac{\rho_f (1 - \phi) |\langle \mathbf{W} \rangle| d_p}{\mu_f},$$

where d_p is the particle diameter, μ_f is the dynamic viscosity of the fluid phase, and $\langle \mathbf{W} \rangle$ is the mean slip velocity between the particles and the fluid.

For each set of physical parameters, five independent realizations (corresponding to a specified initial particle configuration) are simulated in this study. The initial positions of the particles are obtained following elastic collisions (in the absence of interstitial fluid), starting from a lattice arrangement with a Maxwellian velocity distribution. All the mean quantities in the fluid phase are computed by first volume-averaging the flow variable for one realization and, subsequently, ensemble-averaging over different particle realizations. The mean quantities in the dispersed phase are computed by averaging over all particles and then ensemble-averaging over different particle configurations.

Although the primary goal of this work is the simulation of freely evolving suspensions, in order to separate the effects of particle velocity fluctuations, clustering and mobility on the drag of moving particles, we have performed, in total, five different types of simulations which are summarized in Table 1. The base simulations are for fixed assemblies of homogeneous particles (Case 1: Homogeneous Fixed). To show the effect of particle clustering on the drag force, we use the configuration of particles from the simulation of freely evolving suspensions after it reaches a statistically stationary state (steady values of second moments of particle and fluid velocities) and simulate it as a fixed bed of stationary particles (Case 2: Clustered Fixed). Assigning a random fluctuating velocity sampled from moving particle simulations to each particle in the homogeneous fixed bed allows considering the pure effect of particle velocity fluctuations on the hydrodynamic forces (Case 3: Homogeneous Snapshot). If a random fluctuating velocity sampled from moving particle simulations is assigned to each particle in the clustered fixed bed, then the fixed bed simulation can be considered as an instantaneous snapshot of a freely evolving suspension (Case 4: Clustered Snapshot). Of course, in a freely evolving suspension, the dynamic response of the particles to the hydrodynamic forces will affect the particle velocity and position, and this is not captured by the snapshot simulation. We have considered this effect by simulating freely evolving suspensions (Case

5: Freely Evolving).

Table 1: The different types of simulations classified as cases that are considered in this study.

Case	Name	particle configuration	mobility	particle velocity
1	Homogeneous Fixed	homogeneous	stationary	zero
2	Clustered Fixed	clustered	stationary	zero
3	Homogeneous Snapshot	homogeneous	stationary	non-zero
4	Clustered Snapshot	clustered	stationary	non-zero
5	Freely Evolving	clustered	moving	non-zero

The salient numerical and physical parameters used in the simulations are reported in Table 2.

Table 2: The numerical and physical parameters of the simulations: volume fraction of particles ϕ , the number of grid cells across the diameter of a particle $d_p/\Delta x$ (numbers before the "/" correspond to $Re_m < 100$ while numbers after the "/" correspond to $Re_m = 100$), the ratio of the length of the box to the particle diameter L/d_p , number of particles N_p , Reynolds number Re_m , and particle-to-fluid density ratio ρ_p/ρ_f .

ϕ	$d_p/\Delta x$	L/d_p	N_p	Re_m	ρ_p/ρ_f
0.1	20/30	10.16	200	10, 20, 50, 100	0.01, 0.1, 10, 100
0.2	20/30	8.06	200	10, 20, 50, 100	0.01, 0.1, 10, 100
0.3	30/40	7.05	200	10, 20, 50, 100	0.01, 0.1, 10, 100
0.4	30/40	6.4	200	10, 20, 50, 100	0.01, 0.1, 10, 100

4. Results and discussion

4.1. Mean drag force

Figure 1 shows the non-dimensional drag force $F = F_d/F_{st}$ (see Appendix A for details on F_d) as a function of density ratio for different Reynolds numbers and volume fractions in freely evolving suspensions compared to the drag correlation by Tenneti et al. [13] for fixed beds. Here F_d is the dimensional average

drag on each particle and $F_{st} = 3\pi\mu_f(1-\phi)d_p|\langle\mathbf{W}\rangle|$ is Stokes drag. Note that F_d does not include the effect of the mean pressure gradient. The relation between this drag force and total fluid-particle force, which includes the effect of the mean pressure gradient, is explained in Appendix A.

This figure shows that depending on the flow conditions, the drag of a freely evolving suspension could be smaller than, greater than, or the same as in its fixed bed counterpart. To further examine the difference between mean drag in moving particles and fixed beds, we have studied the effects of particle velocity fluctuations, clustering, and mobility in the following subsections.

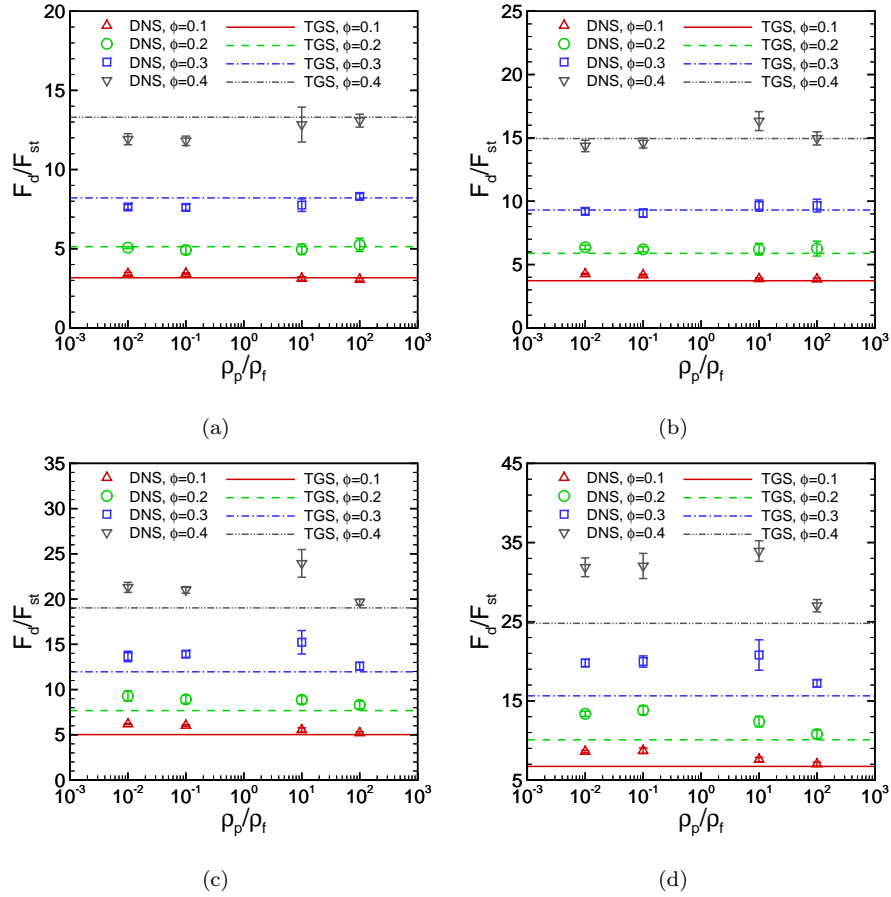


Figure 1: Non-dimensional drag force $F = F_d/F_{st}$, as a function of ρ_p/ρ_f for different Re_m and ϕ . The drag correlation by Tenneti et al. [13], denoted by TGS, for fixed beds, is also shown for comparison. Symbols show PR-DNS data, and lines represent the correlation. The error bars represent 95% confidence intervals obtained from five independent realizations for each case. (a) $Re_m = 10$. (b) $Re_m = 20$. (c) $Re_m = 50$. (d) $Re_m = 100$.

Table 3 summarizes the main conclusions from this study, which are supported by providing the results in the following subsections. It is shown that the presence of the clustering in particle configuration increases the drag by generating horizontal clusters for the range of parameters studied in this work. The particle velocity fluctuations for the homogeneous configuration also increases the drag. However, the effect of particle velocity fluctuations on the drag for

the clustered case does not have a specific trend and could increase or decrease the drag force. This indicates that the effects of clustering and particle velocity fluctuations are not independent. Finally, the mobility of particles decreases the drag.

Table 3: The effects of different factors on drag.

Parameter	Effect on the drag	Quantification
clustering	increase	$F_{\text{fixed}}^{\text{clustered}} - F_{\text{fixed}}^{\text{homogeneous}}$
particle velocity fluctuations (homogeneous)	increase	$F_{\text{snapshot}}^{\text{homogeneous}} - F_{\text{fixed}}^{\text{homogeneous}}$
particle velocity fluctuations (clustered)	increase/decrease	$F_{\text{snapshot}}^{\text{clustered}} - F_{\text{fixed}}^{\text{clustered}}$
mobility	decrease	$F_{\text{moving}}^{\text{clustered}} - F_{\text{snapshot}}^{\text{clustered}}$

4.2. Effect of particle clustering

Figure 2 shows the change in drag of clustered fixed particle configurations (Case 2) in comparison to homogeneous fixed assemblies (Case 1). It shows that the drag of clustered particles increases in comparison with homogeneous cases, which suggests the presence of horizontal clustering or rafts.

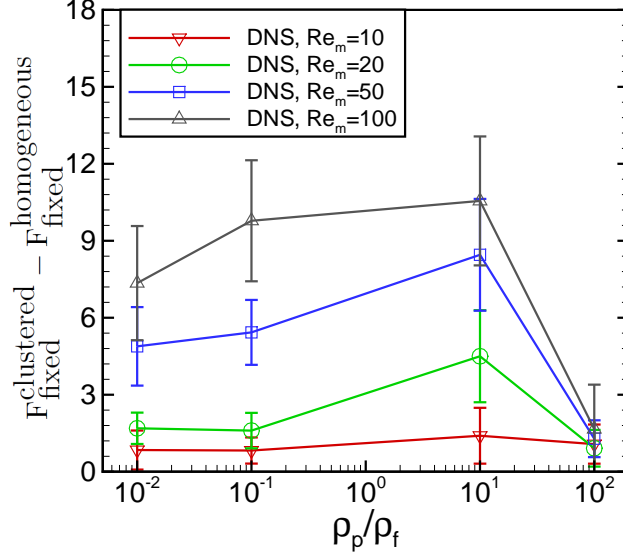


Figure 2: Drag difference scaled with Stokes drag between homogeneous and clustered fixed bed (Cases 1 and 2) as a function of ρ_p/ρ_f for different Re_m and $\phi = 0.4$. The error bars represent 95% confidence intervals obtained from five independent realizations for each case.

To quantify particle clustering in our simulations and explain its connection to the increase in drag, we calculate the radial and angular pair distribution functions which are defined as [61]:

$$g(r) = \frac{V_{sys}}{N_p(N_p - 1)} \frac{1}{\Delta V(r)} \sum_{i=1}^{N_p} \sum_{j=1, i \neq j}^{N_p} \delta \left(r - \frac{1}{2} \Delta r \leq R < r + \frac{1}{2} \Delta r \right),$$

$$g(\theta) = \frac{V_{sys}}{N_p(N_p - 1)} \frac{1}{\Delta V(\theta)} \sum_{i=1}^{N_p} \sum_{j=1, i \neq j}^{N_p} \delta \left(\theta - \frac{1}{2} \Delta \theta \leq \Theta < \theta + \frac{1}{2} \Delta \theta \right),$$

where V_{sys} is the volume of the system, $\Delta V(r)$ is the volume of a spherical shell between $r - \Delta r/2$ and $r + \Delta r/2$, $\Delta V(\theta)$ is the volume of the spherical sector of radius r^* contained within the angles $\theta - \frac{1}{2} \Delta \theta$ and $\theta + \frac{1}{2} \Delta \theta$, R is the distance between the centroids of particles i and j , Θ is the angle between the flow direction and the centerline of particles i and j , and $\delta(\cdot)$ is equal to one if the condition in parentheses is true and zero otherwise.

Figure 3(a) shows the radial pair distribution function for different density

ratios and $Re_m = 50$. The higher peak at low-density ratios indicates larger clusters for buoyant particles and explains the larger difference in the drag seen in Fig. 2. Such a dependence of the peak on density ratio is observed at all Re_m , but not shown here. As r/d_p becomes larger, $g(r)$ goes to one which means at larger scales the distribution of particles in all cases is uniform and particle clustering is happening locally. Figure 3(b) shows the angular pair distribution function for the same cases when $r^* = 1.25d_p$ is chosen. The peak close to $\theta = 90^\circ$ is a sign of horizontal clustering and explains the increase of drag ($\theta = 0^\circ$ is defined in the flow direction). If we use a larger value for r^* , $g(\theta)$ becomes almost uniform and equal to one for all cases, which again shows that particle positions are uncorrelated at larger scales. This observation is consistent with the results for bubbly flows reported in Bunner and Tryggvason [46, 61].

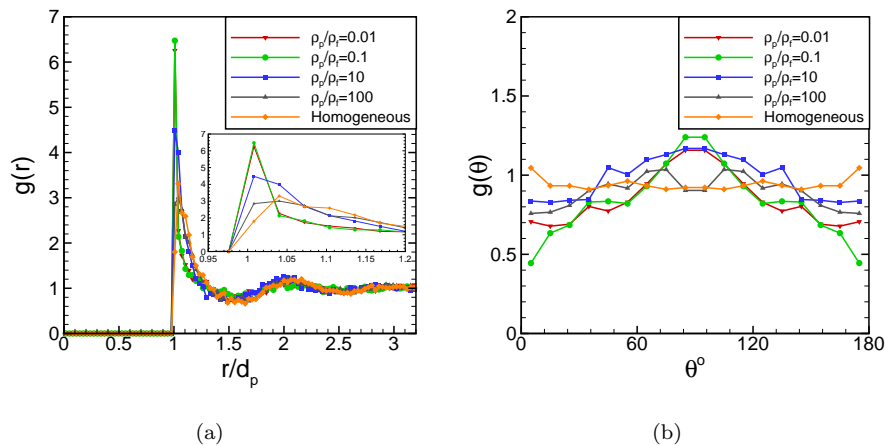


Figure 3: Pair distribution functions for fixed bed (homogeneous) and freely evolving cases with different density ratios at $Re_m = 50$ and $\phi = 0.4$. (a) Radial pair distribution function. (b) Angular pair distribution function with $r^* = 1.25d_p$.

Although Fig. 2 only shows results for $\phi = 0.4$, the increase of drag due to clustering is seen for all cases studied in this work. However, as we mentioned in the Introduction, a decrease in drag due to vertical clustering is reported in the simulation of moving particles in dilute systems ($\phi < 0.01$) at high Reynolds

number ($Re > 200$) [39, 49]. This is because columnar clusters reduce drag but rafts (horizontal) clusters increase drag.

4.3. Effect of particle velocity fluctuations

To characterize the effect of particle velocity fluctuations, it is useful to define a Reynolds number based on the granular temperature as:

$$Re_T = \frac{\rho_f T^{1/2} d_p}{\mu_f},$$

where $T = \langle \mathbf{v}'' \cdot \mathbf{v}'' \rangle / 3$ is the granular temperature and $\mathbf{v}'' = \mathbf{v} - \langle \mathbf{v} \rangle$ denotes the fluctuation in the particle velocity \mathbf{v} with respect to the mean particle velocity $\langle \mathbf{v} \rangle$.

Figure 4 shows the Reynolds number based on the granular temperature at the statistically stationary state for different Re_m and ρ_p/ρ_f . Previous studies have shown that the granular temperature increases continuously with decreasing density for heavy particles ($\rho_p/\rho_f \geq 100$) [36, 39, 58], and reaches an asymptotic value for buoyant particles [54] which is the same trend seen in Fig. 4.

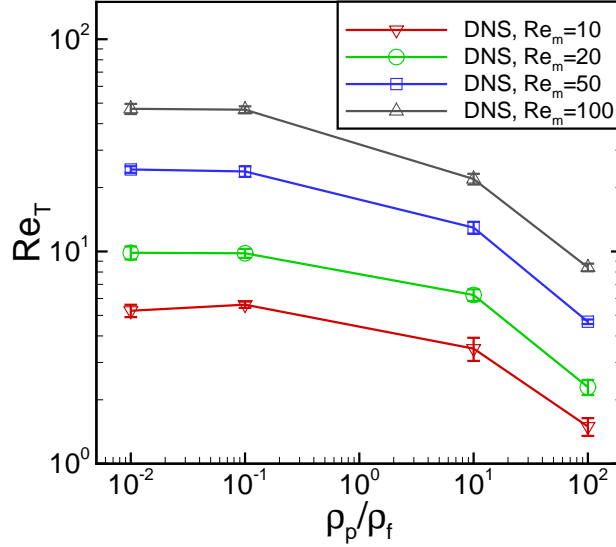


Figure 4: Reynolds number based on the granular temperature Re_T , as a function of ρ_p/ρ_f for different Re_m and $\phi = 0.4$. The error bars represent 95% confidence intervals obtained from five independent realizations for each case.

To study the effect of particle velocity fluctuations on the drag experienced by a homogeneous configuration of particles, we compare the drag of the homogeneous snapshot setup (Case 3) with its homogeneous fixed counterpart (Case 1). Figure 5(a) shows an increase in drag for snapshot simulations when compared to homogeneous fixed beds. The change in drag increases with decreasing density ratio and increasing Reynolds number. This trend corresponds to an increase in particle velocity fluctuations or Re_T , according to Fig. 4. Figure 5(a) also shows the increase of drag due to particle velocity fluctuations from the correlation of Huang et al. [31] for the corresponding Re_m , Re_T , and ϕ . Huang et al. [31] used a similar approach for developing their correlations. However, they assigned a random fluctuating velocity to each particle in the fixed bed according to a Gaussian distribution corresponding to a specified value of the particle granular temperature, while in our simulations, we get the velocity of each particle from the simulation of freely evolving suspensions at the statistically stationary state. Huang’s correlation is developed based on a dataset with

$Re_T < 34.6$, and our results and their correlation match well in this range. For higher values, their correlation overpredicts the increase in drag. Note that we have calculated the value of Huang’s correlation using the equivalent value of Re_T from Fig. 4 for different density ratios.

Similar to the comparison of snapshot and fixed setup of homogeneous beds, we can compare the snapshot and fixed setup for clustered assemblies. Figure 5(b) shows that unlike the homogeneous beds, the change of the drag for clustered snapshot simulations (Case 4) in comparison with clustered fixed beds (Case 2) does not have any specific trend with ρ_p/ρ_f or Re_m . This means that *particle clustering affects the role that particle velocity fluctuations play in the drag force*. In other words, particle clustering affects the drag force both directly (see Section 4.2), and indirectly through particle velocity fluctuations.

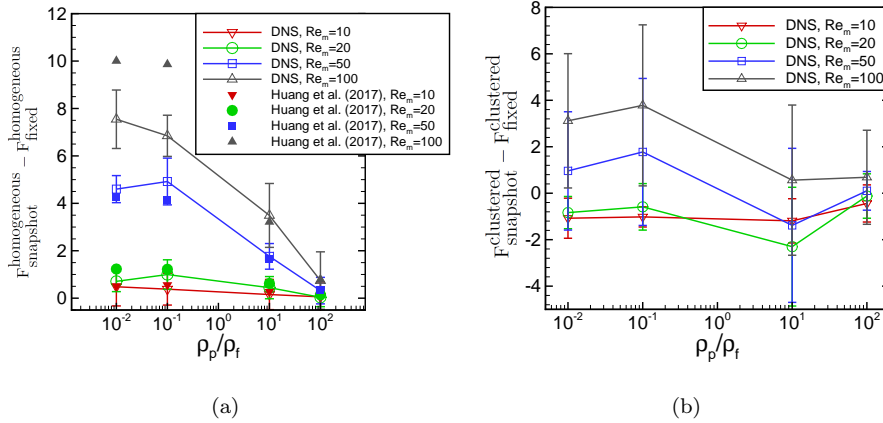


Figure 5: Drag difference scaled with Stokes drag between snapshot and fixed setups, as a function of ρ_p/ρ_f for different Re_m and $\phi = 0.4$. The error bars represent 95% confidence intervals obtained from five independent realizations for each case. The corresponding Re_T of each case in snapshot simulations is shown in Fig. 4. (a) Homogeneous (Cases 1 and 3). The results from the correlation of Huang et al. [31] are also shown for the corresponding Re_m , Re_T , and ϕ for comparison. (b) Clustered (Cases 2 and 4).

4.4. Effect of particle mobility

To study the effect of particle mobility on drag, we have compared the drag of snapshot clustered simulations (Case 4) with freely evolving particles (Case

5). Figure 6 shows a decrease in drag for moving particles when compared to snapshot clustered simulations. The decrease is more significant for buoyant particles, since buoyant particles are more mobile and align their motion immediately with the streamlines of fluid flow.

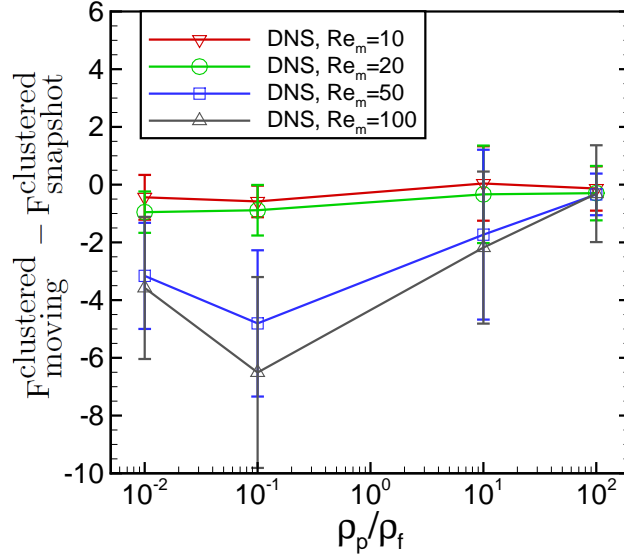


Figure 6: Drag difference scaled with Stokes drag between freely evolving suspension and its snapshot counterpart (Cases 4 and 5), as a function of ρ_p/ρ_f for different Re_m and $\phi = 0.4$. The error bars represent 95% confidence intervals obtained from five independent realizations for each case.

One way to characterize the mobility of particles is by using the particle Stokes number, which is the ratio of the particle momentum response time to the characteristic time of the flow. This number for a single solid particle in the Stokes flow regime is defined as:

$$St = \frac{\rho_p |\langle \mathbf{W} \rangle| d_p}{18\mu_f}.$$

For small Stokes number, the particles follow the streamlines of fluid, and for higher values, they continue moving on their initial trajectory. To account for the effects of volume fraction, finite Reynolds number, and added mass, the

Stokes number is modified as [62]:

$$St = \frac{(\rho_p/\rho_f + C_{am})}{18} \frac{Re_m}{(1 - \phi)} \frac{1}{F_d(Re_m, \phi)}. \quad (1)$$

According to this definition, the Stokes number decreases with decreasing density ratio and reaches a constant value due to the added mass coefficient.

4.5. Discussion on the range of density ratio considered in this study

Before developing a drag law in the next section, it is useful to have a discussion on the physical relevance of the density ratio range ($0.01 \leq \rho_p/\rho_f \leq 100$) studied in this work. This range covers some physical problems, for instance, microplastics, such as polyethylene and polypropylene, in the oceans ($\rho_p/\rho_f \sim 0.9$) [63], different solid particles such as glass or sand in water ($\rho_p/\rho_f \sim \mathcal{O}(1 - 10)$), and cork in the air ($\rho_p/\rho_f \sim 100$) [58]. Obviously, there are some other applications of particle suspensions that are not covered here. Although it might be useful to study a broader range of density ratios, it is computationally expensive. In fact, the most significant variation in the behavior of the system due to the change of density ratio occurs in the range studied here. Therefore the behavior of systems with a density ratio outside the range studied here can be predicted by the data presented in this work.

In fact, Tavanashad et al. [54] simulated particle suspensions with a wider range of density ratio including $\rho_p/\rho_f = 0.001$ and 1000, but only for $Re_m = 20$. Similar to the results presented here, they showed that the results are almost independent of the density ratio for buoyant particles. This means that our conclusions about buoyant particles can be extended to lower density ratios, for example, air bubbles in contaminated water where $\rho_p/\rho_f \sim 0.001$. There are also several industrial application of gas–solid flows with $\rho_p/\rho_f \geq \mathcal{O}(10^3)$. Tavanashad et al. [54] also showed that the mean drag for $\rho_p/\rho_f = 1000$ is in good agreement with the mean drag in fixed beds. Even our results for $\rho_p/\rho_f = 100$ are close to fixed beds. In addition, it is well accepted that granular temperature for heavy particles is proportional to $(\rho_p/\rho_f)^{-1}$ [36, 58]. Overall,

we expect that our conclusions for $\rho_p/\rho_f = 100$ to be applicable to higher density ratios as well.

5. A new drag law for freely evolving suspensions

As mentioned in the Introduction, an accurate drag correlation is essential to perform predictive CFD simulations. In this section, we propose a new drag law for interphase momentum transfer in particle suspensions based on the complete set of freely evolving simulations performed in this work. To develop the correlation, we can follow two different strategies, which are discussed in this section.

5.1. Drag law using symbolic regression

In the first approach, we use symbolic regression to derive a correlation for mean drag. To do this, we have used the HeuristicLab software package [64]. The output of this software is a mathematical expression that fits the input data. Alongside this expression, the model is also presented as a tree where each sub-tree is a term in the expression. For each sub-tree, a *node impact* is defined, which shows the importance of that sub-tree and has a value between zero and one (zero: not important, one: very important). Therefore, the tree (and the corresponding mathematical expression) can be simplified by removing sub-trees that do not significantly affect the accuracy of the model. Usually, the original expression provided by the software is long and complicated; therefore, it is necessary to simplify the model to come up with a simpler expression. In developing our correlation, we have eliminated sub-trees which have a *node impact* smaller than 0.001. In this software, we also have the option to choose the functional forms which can be used in developing the model such as polynomial power functions, exponential functions, and logarithmic functions.

To develop the correlation, we have to specify which variables the drag correlation should depend on. In previous works, three different sets of variables have been used. Tang et al. [36] proposed a correlation in the form of $F(Re_m, \phi, Re_T)$.

Rubinstein et al. [37] used $F(\phi, St)$ format for low Reynolds flows, so their correlation does not depend on Re_m . The correlation by Zaidi [39] is in the form of $F(Re_m, \phi, \rho_p/\rho_f)$. Note that the variables in these correlations are not independent: $Re_m(\phi)$, $Re_T(Re_m, \phi, \rho_p/\rho_f)$, and $St(Re_m, \phi, \rho_p/\rho_f)$.

At the outset it is not clear which is the best choice for the set of independent variables. In general, assuming \mathbf{x} , \mathbf{y} , and \mathbf{z} represent the different independent variable spaces, we can formulate correlations as $f_1(x_1, x_2, x_3)$, $f_2(y_1, y_2, y_3)$, and $f_3(z_1, z_2, z_3)$, while recognizing that $\mathbf{y} = u(\mathbf{x})$ and $\mathbf{z} = w(\mathbf{x})$. We now examine which choice is the best and what are the performance metrics for comparing three different approaches. To answer these questions, we have developed correlations in three spaces $(Re_m, \phi, \rho_p/\rho_f)$, (Re_m, ϕ, Re_T) , and (Re_m, ϕ, St) which already have been used in the literature. It is also possible to define new variable spaces using data-driven dimensional analysis by measuring the relative importance of variables [65], which is the subject of further studies.

The performance metrics we consider in this work to compare these three variable spaces are complexity, accuracy, and predictability. We divide the input data randomly into 80% training and 20% test datasets. The training dataset is used to measure the accuracy of the correlation by considering the average and maximum relative error between the correlations and data points. Using the same criterion, the test dataset is used to measure the predictability of the correlation. The complexity of each correlation is measured by considering the number of model constants in the correlation.

Table 4 summarizes the features/performance of different correlations. Although there is not a meaningful difference between the performance of the three correlations, the one which is a function of density ratio has a smaller error for both training and test datasets with fewer constants in the correlation. This variable space also has the benefit that ρ_p/ρ_f is an input parameter while Re_T and St are derived quantities.

Table 4: Comparison of correlations developed for drag law using different variable spaces.

Parameter	Complexity	Accuracy		Predictability	
Criterion	Number of constants	relative error of training dataset		relative error of test dataset	
		Avg (%)	Max (%)	Avg (%)	Max (%)
$F(Re_m, \phi, \rho_p/\rho_f)$	12	4.41	18.26	4.70	13.18
$F(Re_m, \phi, Re_T)$	12	4.99	13.14	6.74	17.05
$F(Re_m, \phi, St)$	19	5.43	20.12	5.50	10.99

Although using symbolic regression is straightforward, one may encounter some problem using this approach since we do not have so much control over the final functional form of the correlation. For instance, the model developed in this approach is only valid in the range of input data used. This is not a problem by itself, and of course, is to be expected. However, the final goal of developing such correlations is to use them in large scale simulations such as EE or EL, which are used for systems with a very wide range of parameters. So it is important that the proposed correlations at least show a reasonable trend when they are used out of their proposed range. For the drag law of freely evolving suspensions, it is important that the proposed correlation converges to the drag of fixed beds for large values of density ratios, and goes to zero with decreasing volume fraction. To overcome these problems, we included the data for fixed beds in our input dataset. Besides, we added a few additional data points based on the physics to better satisfy the limiting cases such as zero drag at $\phi = 0$. By considering these modifications, our final correlation is (See Appendix B for a corrigendum)

$$\begin{aligned}
 F(Re_m, \phi, \rho_p/\rho_f) = F_d/F_{st} = & c_1 + c_2 \phi + c_3 \phi Re_m + c_4 \phi^5 Re_m^{1/3} \\
 & + \frac{c_5 + Re_m + c_6 \phi Re_m^2}{c_7 + c_8 \rho_p/\rho_f}
 \end{aligned} \tag{2}$$

with the following constants,

$$\begin{aligned}c_1 &= 0.245, & c_2 &= 22.8, & c_3 &= 0.242, & c_4 &= 130.371, \\c_5 &= 6.708, & c_6 &= 0.233, & c_7 &= 140.272, & c_8 &= 2.299,\end{aligned}$$

which fits the data with a relative error less than 24%.

Figure 7 shows the non-dimensional drag force $F = F_d/F_{st}$, as a function of density ratio for different Reynolds numbers and volume fractions from PR-DNS and the new drag correlation, i.e. Eq. (2), for comparison.

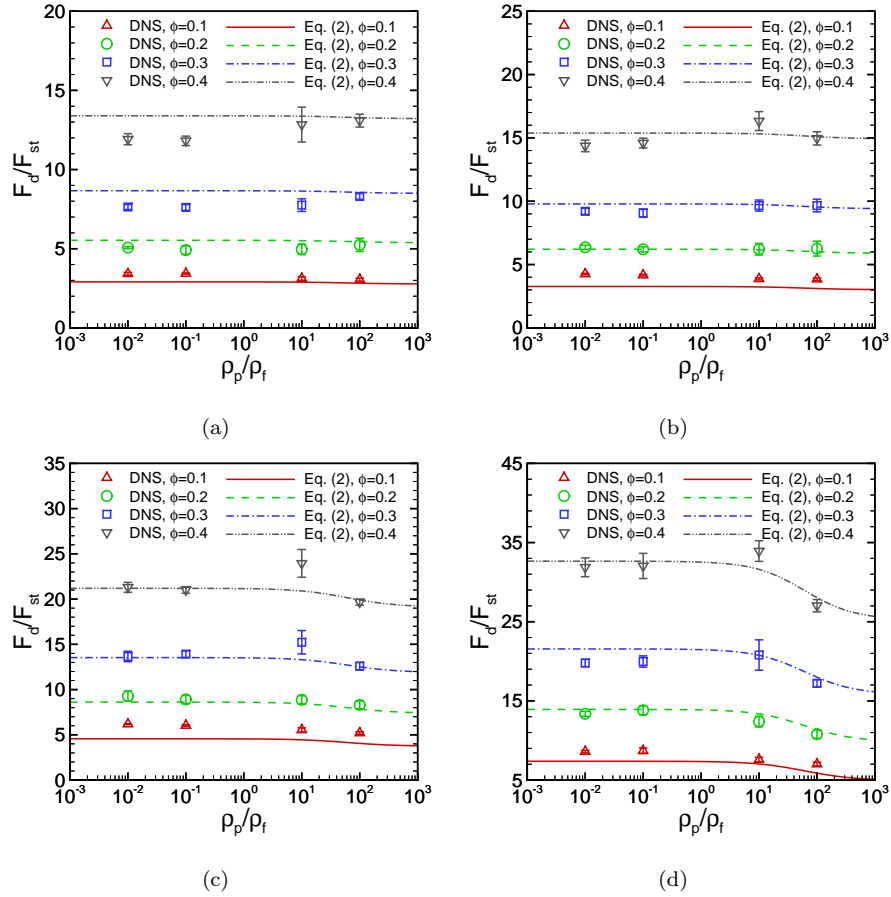


Figure 7: Non-dimensional drag force $F = F_d/F_{st}$, as a function of ρ_p/ρ_f for different Re_m and ϕ . The drag correlation by Eq. (2) is also shown for comparison. Symbols show PR-DNS data, and lines present the correlation. The error bars represent 95% confidence intervals obtained from five independent realizations for each case. (a) $Re_m = 10$. (b) $Re_m = 20$. (c) $Re_m = 50$. (d) $Re_m = 100$.

Before finishing this subsection, we want to mention other problems with symbolic regression, which one may encounter. It is possible that the developed correlation is singular for specific combinations of Re_m , ϕ , and ρ_p/ρ_f if this results in a zero value in the denominator. Our correlation becomes singular for a negative value of density ratio, which is not a problem. Another problem with symbolic regression is that the results are not reproducible, which means that

every time we run the software, we may come up with a different model. This is because of the use of genetic algorithm, which is an stochastic search algorithm, in symbolic regression. Considering all these possible difficulties/problems with symbolic regressions, we discuss proposing correlations using a predefined functional form in the next subsection.

5.2. Drag law using predefined functional forms

The second approach for developing drag correlations is using a predefined functional form for the correlation, which is informed by the physics of the problem. Generally, the correlations used to describe the drag force in general flow conditions are classified into two forms. In the first approach, the correlation is based on the drag force in the limit of Stokes flow regime to which a term linear in Re_m is added accounting for the inertial effects,

$$F_d(Re_m, \phi) = F_d(0, \phi) + \alpha Re_m. \quad (3)$$

Originally, α was only a function of volume fraction [66]. However, it was later shown that α also depends on Re_m [13, 15, 17]. Recently, Tang et al. [36] proposed a drag law for moving particles by adding a term to their fixed bed correlation [21]. In other words, they proposed a correlation for the change of drag in moving particles in comparison to its fixed bed counterpart.

Although it seems more convenient to use Tang's form of the correlation for incorporating the particle motion in fixed bed drag laws, we could not find a simple and accurate model for ΔF for our dataset using symbolic regression.

In the second form of drag laws, the relation is based on the drag force on a single particle, where the influence of the other particles is accounted for by multiplying with a power of the voidage,

$$F_d(Re_m, \phi) = F_d(Re_m, 0) (1 - \phi)^{-n}. \quad (4)$$

The value of n was originally constant [67] but it was later shown that it is also a function of Reynolds number [18, 68]. Most recently, Zaidi [39] showed that

the dependence of n on density ratio should also be considered for heavy moving particles.

To utilize this form of the drag law, we use the Schiller–Naumann drag law for $F_d(Re_m, 0)$, i.e.,

$$F_d(Re_m, 0) = F_{single} = F_{st} (1 + 0.15Re_m^{0.687}). \quad (5)$$

The results with this new scaling are presented in Fig. 8. Interestingly, the results for all Reynolds number and $\rho_p/\rho_f \leq 10$ approximately collapse to a single line. This means for this range of parameters; the new scaled drag is only a function of volume fraction. However, the new scaled drag for $\rho_p/\rho_f = 100$ shows a dependence on Reynolds number in addition to ϕ (see Fig. 8(b)). In Fig. 8(b), the drag for fixed beds with this new scaling is also shown. It is clear that the drag of fixed beds is close to the drag of moving particles for $\rho_p/\rho_f = 100$. By curve fitting using MATLAB, and using the fact that F_d/F_{single} should be unity at $\phi = 0$, we will have ($R^2 = 0.9852$):

$$\frac{F_d}{F_{single}} = (78.96\phi^3 - 18.63\phi^2 + 9.845\phi + 1)^n. \quad (6)$$

where $n = 1$ for light particles with $\rho_p/\rho_f \leq 10$ (liquid–solid and bubbly flows). To improve this correlation for gas–solid flows $\rho_p/\rho_f = 100$, we propose the following expression for n which is inspired by Garside and Al-Dibouni [69],

$$\frac{1.05 - n}{n - 0.9} = 4.3 \times 10^{-4} Re_m^{2.361}. \quad (7)$$

The correlation given by Eqs. (6) and (7) fits the data with a relative error less than 14% which is an improvement over the correlation presented by Eq. (2). Also note that comparing Eqs. (4) and (6), we have used a third degree polynomial instead of $(1 - \phi)^{-1}$ to get a better fit.

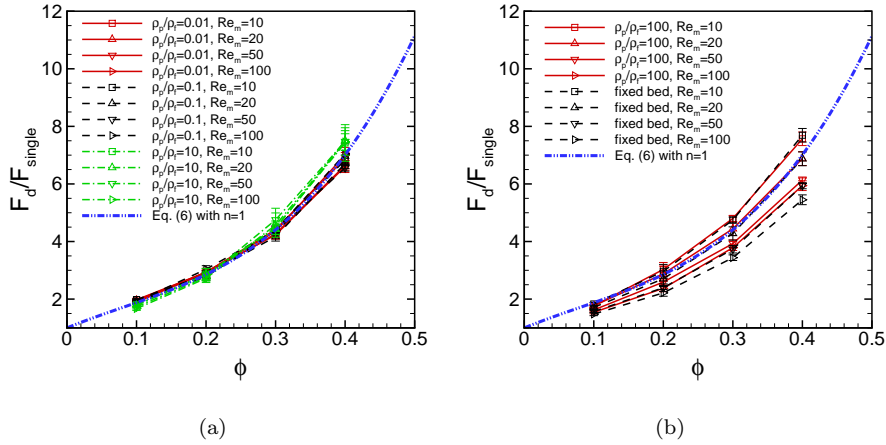


Figure 8: Non-dimensional drag force F_d/F_{single} , as a function of ϕ for different Re_m and ρ_p/ρ_f . The drag correlation by Eq. (6) is also shown for comparison. Symbols show PR-DNS data, and lines present the correlation. The error bars represent 95% confidence intervals obtained from five independent realizations for each case. (a) $\rho_p/\rho_f = 0.01, 0.1, 10$. (b) $\rho_p/\rho_f = 100$ and fixed beds.

Generally, the drag law is used to model the unclosed average interphase momentum transfer term in the mean momentum conservation equation of the two-fluid theory, and determines the overall mean particle-laden flow structure. Since our drag law is inferred from freely evolving particle suspensions, the effect of the motion of the particles is captured in the drag correlation. This improved drag law can enhance the predictive capability of CFD simulations of particle-laden flows that are based on the two-fluid theory. The improved drag law can also be used to refine the stability limits for particle-laden suspensions since these limits are determined by the functional dependence of drag on volume fraction.

Before concluding our work, we want to emphasize two points. First, our correlations apply to homogeneous flows. Although we discussed the clustering of particles in Section 4.2, this clustering, as we mentioned earlier, only happens at small scales (less than $1.5d_p$) and we call it *short-range clustering*, in contrast to, long-range clustering in gas–solid flows where the length scale of clusters is $O(10 - 100)d_p$ [70]. This means that particles are dispersed approximately

homogeneously in the domain at large scales, which is consistent with previous works on bubbly flows [46, 61]. Second, the focus of this work is on the effect of motion of particles on the drag compared to fixed beds. However, another important topic in particle-laden flows is the distribution of force on different particles [31, 71, 72] which is an essential consideration in developing stochastic [58, 72, 73] or deterministic [74–76] models for point-particle simulations.

6. Conclusions

PR-DNS are performed for a wide range of Reynolds number ($10 \leq Re_m \leq 100$), volume fraction ($0.1 \leq \phi \leq 0.4$), and density ratio ($0.01 \leq \rho_p/\rho_f \leq 100$). The effects of particle clustering, particle velocity fluctuations, and mobility of particles on the interphase momentum transfer of dispersed multiphase flows are studied. It is shown that clustering in the particle configuration increases the drag by generating a horizontal raft. Although particle velocity fluctuations characterized by the Reynolds number based on granular temperature increase the drag for homogeneous configurations, it is shown that the effects of particle clustering and particle velocity fluctuations are not independent. Overall, the combined effects of particle clustering and particle velocity fluctuations decrease or increase the drag depending on flow conditions. It is also found that the mobility of particles decreases the drag. Finally, it is shown that the competing effects of these factors could result in an increase, decrease, or no change of drag in freely evolving suspensions in comparison to fixed beds.

A new drag law for monodisperse suspensions is proposed using two different approaches: symbolic regression and predefined functional forms. In the symbolic approach, the correlation is proposed as a function of $F(Re_m, \phi, \rho_p/\rho_f)$ to incur the least error for both training and test datasets with a fewer number of constants in the correlation in comparison with other variable spaces. It is also shown that we can develop a correlation using predefined functional forms which only depend on volume fraction for $\rho_p/\rho_f \leq 10$.

Acknowledgment

This material is based upon work supported by the National Science Foundation under Grant no. CBET 1438143.

Appendix A. Drag force and total fluid-particle drag

At the statistically stationary state, each particle experiences two forces from the fluid, a body force \mathbf{F}_{mpg} due to mean pressure gradient and a force \mathbf{F}_d resulting from the fluctuating pressure field and the viscous contribution to the drag force. The sum of these two forces is the total fluid-particle force $\mathbf{F}_{g \rightarrow s}$ that the fluid exerts on a particle. The forces are related to the pressure drop over the system as follow:

$$-\langle \nabla P \rangle_v = \frac{N_p}{\mathbf{V}_{sys}} \mathbf{F}_{g \rightarrow s} = \frac{N_p}{\mathbf{V}_{sys}} (\mathbf{F}_d - V_p \langle \nabla P \rangle_v), \quad (\text{A.1})$$

where V_p is the volume of a single particle. Eq. A.1 can be written as:

$$-\langle \nabla P \rangle_v = \frac{\phi}{1 - \phi} \frac{\mathbf{F}_d}{V_p}. \quad (\text{A.2})$$

From Eqs. (A.1) and (A.2), it follows that,

$$\begin{aligned} \mathbf{F}_{g \rightarrow s} &= \mathbf{F}_d + \mathbf{F}_{mpg} = \mathbf{F}_d - \langle \nabla P \rangle_v V_p, \\ \mathbf{F}_{mpg} &= \frac{\phi}{1 - \phi} \mathbf{F}_d, \\ \mathbf{F}_{g \rightarrow s} &= \frac{\mathbf{F}_d}{1 - \phi} = \frac{\mathbf{F}_{mpg}}{\phi}. \end{aligned} \quad (\text{A.3})$$

In PR-DNS, \mathbf{F}_d and $\mathbf{F}_{g \rightarrow s}$ are calculated by averaging over all the particles. In the literature, both \mathbf{F}_d [16, 17, 54] and $\mathbf{F}_{g \rightarrow s}$ [13–15, 21] are reported for proposing drag laws, and their relation is $(1 - \phi) \mathbf{F}_{g \rightarrow s} = \mathbf{F}_d$ as shown in Eq. (A.3). In this work, we have reported $|\mathbf{F}_d|$.

Appendix B. Corrigendum

The authors would like to draw attention to the fact that the drag correlation presented in Section 5.1 by Eq. (2) converges to almost zero for the limit of zero

volume fraction. However, it should converge to the drag on a single particle in this limit. To correct this trend, we define the p -norm of the drag on an isolated particle f_{iso} and the proposed correlation in the article for finite volume fractions f_ϕ as the modified drag correlation,

$$F(Re_m, \phi, \rho_p/\rho_f) = F_d/F_{st} = \left(f_{iso}^p + f_\phi^p \right)^{(1/p)} \quad (\text{B.1})$$

where $f_{iso} = (1 + 0.15Re_m^{0.687})$ is calculated from the well-known Schiller–Naumann drag law and f_ϕ is the drag correlation given in the original paper for finite volume fractions, i.e., Eq. (2), which is repeated here

$$f_\phi = c_1 + c_2 \phi + c_3 \phi Re_m + c_4 \phi^5 Re_m^{1/3} + \frac{c_5 + Re_m + c_6 \phi Re_m^2}{c_7 + c_8 \rho_p/\rho_f}$$

with the following constants,

$$c_1 = 0.245, \quad c_2 = 22.8, \quad c_3 = 0.242, \quad c_4 = 130.371, \\ c_5 = 6.708, \quad c_6 = 0.233, \quad c_7 = 140.272, \quad c_8 = 2.299.$$

With a proper choice of p in Eq. B.1, the p -norm will converges to f_{iso} at low volume fraction since $f_{iso} > f_\phi$ for small volume fractions and it converges to f_ϕ for $\phi \geq 0.1$ since $f_\phi > f_{iso}$ in this range. Our numerical experiments show that the desired behavior is observed for $p = 5$. As indicated, this new modified correlation is technically the same as the original correlation for $\phi \geq 0.1$; therefore, the figures in the article do not change.

For the sake of completeness, we present Fig. B.9 here which compares the behavior of the original and modified correlations as a function of volume fraction for $\rho_p/\rho_f = 0.01$ and $Re_m = 10$ and 100 .

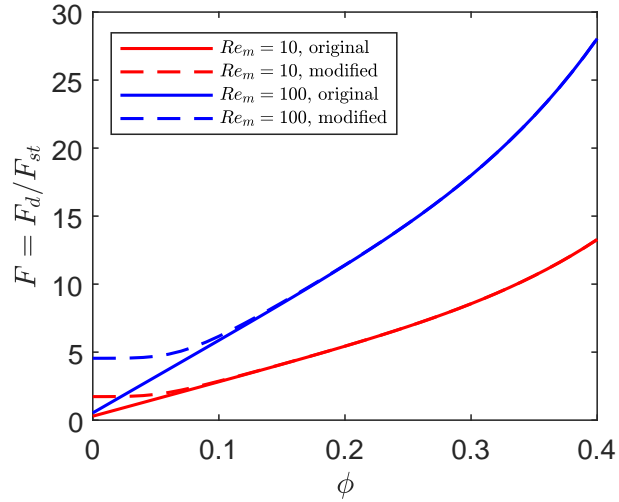


Figure B.9: The comparison between the modified drag correlation (Eq. (B.1)) with $p = 5$ and the original one (Eq. (2)) for $\rho_p/\rho_f = 0.01$ and $Re_m = 10$ and 100 .

References

- [1] Tenneti S, Subramaniam S. Particle-resolved direct numerical simulation for gas–solid flow model development. *Annu Rev Fluid Mech* 2014;46(1):199–230. doi:10.1146/annurev-fluid-010313-141344.
- [2] Tryggvason G, Dabiri S, Aboulhasanzadeh B, Lu J. Multiscale considerations in direct numerical simulations of multiphase flows. *Phys Fluids* 2013;25(3):031302. doi:10.1063/1.4793543.
- [3] Capecelatro J, Desjardins O. An Euler–Lagrange strategy for simulating particle-laden flows. *J Comput Phys* 2013;238:1–31. doi:10.1016/j.jcp.2012.12.015.
- [4] Subramaniam S, Balachandar S. Towards combined deterministic and statistical approaches to modeling dispersed multiphase flows. In: Basu S, Agarwal AK, Mukhopadhyay A, Patel C, editors. *Droplets and Sprays: Applications for Combustion and Propulsion*. Singa-

pore: Springer Singapore. ISBN 978-981-10-7449-3; 2018, p. 7–42.
doi:10.1007/978-981-10-7449-3_2.

- [5] Ishii M. Thermo-fluid dynamics of two-phase flow. Eyrolles Paris; 1975.
- [6] Anderson TB, Jackson R. Fluid mechanical description of fluidized beds. Equations of motion. *Ind Eng Chem Fundamen* 1967;6(4):527–39. doi:10.1021/i160024a007.
- [7] Jackson R. Locally averaged equations of motion for a mixture of identical spherical particles and a Newtonian fluid. *Chem Eng Sci* 1997;52(15):2457–69. doi:10.1016/S0009-2509(97)00065-1.
- [8] Drew DA. Mathematical modeling of two-phase flow. *Annu Rev Fluid Mech* 1983;15(1):261–91. doi:10.1146/annurev.fl.15.010183.001401.
- [9] Drew DA, Passman SL. *Theory of Multicomponent Fluids*. Springer New York; 1999. doi:10.1007/b97678.
- [10] Pai MG, Subramaniam S. A comprehensive probability density function formalism for multiphase flows. *J Fluid Mech* 2009;628:181–228. doi:10.1017/S002211200900617X.
- [11] Joseph D, Lundgren T, Jackson R, Saville D. Ensemble averaged and mixture theory equations for incompressible fluid-particle suspensions. *Int J Multiph Flow* 1990;16(1):35–42. doi:10.1016/0301-9322(90)90035-H.
- [12] Subramaniam S. Multiphase flows: rich physics, challenging theory, and big simulations. *Phys Rev Fluids* 2020;doi:10.13140/RG.2.2.28950.16960; Submitted.
- [13] Tenneti S, Garg R, Subramaniam S. Drag law for monodisperse gas–solid systems using particle-resolved direct numerical simulation of flow past fixed assemblies of spheres. *Int J Multiph Flow* 2011;37(9):1072–92. doi:10.1016/j.ijmultiphaseflow.2011.05.010.

- [14] Hill RJ, Koch DL, Ladd AJC. The first effects of fluid inertia on flows in ordered and random arrays of spheres. *J Fluid Mech* 2001;448:213–41. doi:10.1017/S0022112001005948.
- [15] Hill RJ, Koch DL, Ladd AJC. Moderate-Reynolds-number flows in ordered and random arrays of spheres. *J Fluid Mech* 2001;448:243–78. doi:10.1017/S0022112001005936.
- [16] van der Hoef MA, Beetstra R, Kuipers JAM. Lattice-Boltzmann simulations of low-Reynolds-number flow past mono- and bidisperse arrays of spheres: results for the permeability and drag force. *J Fluid Mech* 2005;528:233–54. doi:10.1017/S0022112004003295.
- [17] Beetstra R, van der Hoef MA, Kuipers JAM. Drag force of intermediate Reynolds number flow past mono- and bidisperse arrays of spheres. *AIChE J* 2007;53(2):489–501. doi:10.1002/aic.11065.
- [18] Rong L, Dong K, Yu A. Lattice-Boltzmann simulation of fluid flow through packed beds of uniform spheres: effect of porosity. *Chem Eng Sci* 2013;99:44–58. doi:10.1016/j.ces.2013.05.036.
- [19] Zaidi AA, Tsuji T, Tanaka T. A new relation of drag force for high Stokes number monodisperse spheres by direct numerical simulation. *Adv Powder Technol* 2014;25(6):1860–71. doi:10.1016/j.apt.2014.07.019.
- [20] Bogner S, Mohanty S, Rde U. Drag correlation for dilute and moderately dense fluid-particle systems using the lattice Boltzmann method. *Int J Multiph Flow* 2015;68:71–9. doi:10.1016/j.ijmultiphaseflow.2014.10.001.
- [21] Tang Y, Peters EAJF, Kuipers JAM, Kriebitzsch SHL, van der Hoef MA. A new drag correlation from fully resolved simulations of flow past monodisperse static arrays of spheres. *AIChE J* 2015;61(2):688–98. doi:10.1002/aic.14645.
- [22] Kravets B, Rosemann T, Reinecke S, Kruggel-Emden H. A new drag force and heat transfer correlation derived from direct numerical

- LBM-simulations of flow through particle packings. *Powder Technol* 2019;345:438–56. doi:10.1016/j.powtec.2019.01.028.
- [23] Yin X, Sundaresan S. Drag law for bidisperse gas–solid suspensions containing equally sized spheres. *iecr* 2009;48(1):227–41. doi:10.1021/ie800171p.
- [24] Yin X, Sundaresan S. Fluid-particle drag in low-Reynolds-number polydisperse gas–solid suspensions. *AIChE J* 2009;55(6):1352–68. doi:10.1002/aic.11800.
- [25] Mehrabadi M, Tenneti S, Subramaniam S. Importance of the fluid-particle drag model in predicting segregation in bidisperse gas–solid flow. *Int J Multiph Flow* 2016;86:99–114. doi:10.1016/j.ijmultiphaseflow.2016.07.006.
- [26] Mehrabadi M, Murphy E, Subramaniam S. Development of a gas–solid drag law for clustered particles using particle-resolved direct numerical simulation. *Chem Eng Sci* 2016;152:199–212. doi:10.1016/j.ces.2016.06.006.
- [27] Wang X, Liu K, You C. Drag force model corrections based on nonuniform particle distributions in multi-particle systems. *Powder Technol* 2011;209(1):112–8. doi:10.1016/j.powtec.2011.02.018.
- [28] Zhou G, Xiong Q, Wang L, Wang X, Ren X, Ge W. Structure-dependent drag in gas–solid flows studied with direct numerical simulation. *Chem Eng Sci* 2014;116:9–22. doi:10.1016/j.ces.2014.04.025.
- [29] Tenneti S, Garg R, Hrenya C, Fox R, Subramaniam S. Direct numerical simulation of gas–solid suspensions at moderate Reynolds number: quantifying the coupling between hydrodynamic forces and particle velocity fluctuations. *Powder Technol* 2010;203(1):57–69. doi:10.1016/j.powtec.2010.03.042.
- [30] Wylie JJ, Koch DL, Ladd AJC. Rheology of suspensions with high particle inertia and moderate fluid inertia. *J Fluid Mech* 2003;480:95–118. doi:10.1017/S0022112002003531.

- [31] Huang Z, Wang H, Zhou Q, Li T. Effects of granular temperature on inter-phase drag in gas–solid flows. *Powder Technol* 2017;321:435–43. doi:10.1016/j.powtec.2017.08.035.
- [32] Balachandar S. Lagrangian and Eulerian drag models that are consistent between Euler–Lagrange and Euler–Euler (two-fluid) approaches for homogeneous systems. *Phys Rev Fluids* 2020;5:084302. doi:10.1103/PhysRevFluids.5.084302.
- [33] Huang Z, Zhang C, Jiang M, Wang H, Zhou Q. Effects of particle velocity fluctuations on inter-phase heat transfer in gas–solid flows. *Chem Eng Sci* 2019;206:375–86. doi:10.1016/j.ces.2019.05.047.
- [34] Kriebitzsch S, van der Hoef M, Kuipers J. Fully resolved simulation of a gas-fluidized bed: a critical test of DEM models. *Chem Eng Sci* 2013;91:1–4. doi:10.1016/j.ces.2012.12.038.
- [35] Luo K, Tan J, Wang Z, Fan J. Particle-resolved direct numerical simulation of gas–solid dynamics in experimental fluidized beds. *AIChE J* 2016;62(6):1917–32. doi:10.1002/aic.15186.
- [36] Tang Y, Peters EAJF, Kuipers JAM. Direct numerical simulations of dynamic gas–solid suspensions. *AIChE J* 2016;62(6):1958–69. doi:10.1002/aic.15197.
- [37] Rubinstein GJ, Derksen JJ, Sundaresan S. Lattice Boltzmann simulations of low-Reynolds-number flow past fluidized spheres: effect of Stokes number on drag force. *J Fluid Mech* 2016;788:576–601. doi:10.1017/jfm.2015.679.
- [38] Rubinstein GJ, Ozel A, Yin X, Derksen JJ, Sundaresan S. Lattice Boltzmann simulations of low-Reynolds-number flows past fluidized spheres: effect of inhomogeneities on the drag force. *J Fluid Mech* 2017;833:599–630. doi:10.1017/jfm.2017.705.

- [39] Zaidi AA. Study of particle inertia effects on drag force of finite sized particles in settling process. *Chem Eng Res Des* 2018;132:714–28. doi:10.1016/j.cherd.2018.02.013.
- [40] Tavanashad V, Subramaniam S. Fully resolved simulation of dense suspensions of freely evolving buoyant particles using an improved immersed boundary method. *Int J Multiph Flow* 2020;132:103396. doi:10.1016/j.ijmultiphaseflow.2020.103396.
- [41] Clift R, Grace JR, Weber ME. *Bubbles, Drops, and Particles*. New York: Academic Press; 1978.
- [42] Magnaudet J, Eames I. The motion of high-Reynolds-number bubbles in inhomogeneous flows. *Annu Rev Fluid Mech* 2000;32(1):659–708. doi:10.1146/annurev.fluid.32.1.659.
- [43] Takagi S, Matsumoto Y. Surfactant effects on bubble motion and bubbly flows. *Annu Rev Fluid Mech* 2011;43(1):615–36. doi:10.1146/annurev-fluid-122109-160756.
- [44] Gillissen JJJ, Sundaresan S, Van Den Akker HEA. A lattice Boltzmann study on the drag force in bubble swarms. *J Fluid Mech* 2011;679:101–21. doi:10.1017/jfm.2011.125.
- [45] Roghair I, Van Sint Annaland M, Kuipers HJAM. Drag force and clustering in bubble swarms. *AIChE J* 2013;59(5):1791–800. doi:10.1002/aic.13949.
- [46] Bunner B, Tryggvason G. Dynamics of homogeneous bubbly flows part 1. Rise velocity and microstructure of the bubbles. *J Fluid Mech* 2002;466:17–52. doi:10.1017/S0022112002001179.
- [47] Esmaeeli A, Tryggvason G. A direct numerical simulation study of the buoyant rise of bubbles at $O(100)$ Reynolds number. *Phys Fluids* 2005;17(9):093303. doi:10.1063/1.2056617.

- [48] Yin X, Koch DL. Lattice-Boltzmann simulation of finite Reynolds number buoyancy-driven bubbly flows in periodic and wall-bounded domains. *Phys Fluids* 2008;20(10):103304. doi:10.1063/1.3001728.
- [49] Uhlmann M, Doychev T. Sedimentation of a dilute suspension of rigid spheres at intermediate Galileo numbers: the effect of clustering upon the particle motion. *J Fluid Mech* 2014;752:310–48. doi:10.1017/jfm.2014.330.
- [50] Sundaresan S, Ozel A, Kolehmainen J. Toward constitutive models for momentum, species, and energy transport in gas-particle flows. *Annu Rev Chem Biomol Eng* 2018;9(1):61–81. doi:10.1146/annurev-chembioeng-060817-084025.
- [51] Mehrabadi M, Subramaniam S. Mechanism of kinetic energy transfer in homogeneous bidisperse gas–solid flow and its implications for segregation. *Phys Fluids* 2017;29(2):020714. doi:10.1063/1.4974502.
- [52] Risso F. Agitation, mixing, and transfers induced by bubbles. *Annu Rev Fluid Mech* 2018;50(1):25–48. doi:10.1146/annurev-fluid-122316-045003.
- [53] Wang J. Effect of granular temperature and solid concentration fluctuation on the gas–solid drag force: a CFD test. *Chem Eng Sci* 2017;168:11–4. doi:10.1016/j.ces.2017.04.031.
- [54] Tavanashad V, Passalacqua A, Fox RO, Subramaniam S. Effect of density ratio on velocity fluctuations in dispersed multiphase flow from simulations of finite-size particles. *Acta Mech* 2019;230:469–84. doi:10.1007/s00707-018-2267-3.
- [55] Mohd-Yusof J. Interaction of massive particles with turbulence. Ph.D. thesis; Cornell University; 1996.
- [56] Garg R, Tenneti S, Mohd-Yusof J, Subramaniam S. Direct numerical simulation of gas–solids flow based on the immersed boundary method. In:

- Pannala S, Syamlal M, O'Brien TJ, editors. Computational Gas-Solids Flows and Reacting Systems: Theory, Methods and Practice. Hershey, PA: IGI Global; 2011, p. 245–76. doi:10.4018/978-1-61520-651-3.ch008.
- [57] Mehrabadi M, Tenneti S, Garg R, Subramaniam S. Pseudo-turbulent gas-phase velocity fluctuations in homogeneous gas-solid flow: fixed particle assemblies and freely evolving suspensions. *J Fluid Mech* 2015;770:210–46. doi:10.1017/jfm.2015.146.
- [58] Tenneti S, Mehrabadi M, Subramaniam S. Stochastic Lagrangian model for hydrodynamic acceleration of inertial particles in gas-solid suspensions. *J Fluid Mech* 2016;788:695–729. doi:10.1017/jfm.2015.693.
- [59] Cundall PA, Strack ODL. A discrete numerical model for granular assemblies. *Géotechnique* 1979;29(1):47–65. doi:10.1680/geot.1979.29.1.47.
- [60] Schwarz S, Kempe T, Fröhlich J. A temporal discretization scheme to compute the motion of light particles in viscous flows by an immersed boundary method. *J Comput Phys* 2015;281:591–613. doi:10.1016/j.jcp.2014.10.039.
- [61] Bunner B, Tryggvason G. Effect of bubble deformation on the properties of bubbly flows. *J Fluid Mech* 2003;495:77–118. doi:10.1017/S0022112003006293.
- [62] Balachandar S. A scaling analysis for point-particle approaches to turbulent multiphase flows. *Int J Multiph Flow* 2009;35(9):801–10. doi:10.1016/j.ijmultiphaseflow.2009.02.013.
- [63] Driedger AG, Dürr HH, Mitchell K, Cappellen PV. Plastic debris in the Laurentian Great Lakes: a review. *J Great Lakes Res* 2015;41(1):9–19. doi:10.1016/j.jglr.2014.12.020.
- [64] Wagner S, Kronberger G, Beham A, Kommenda M, Scheibenpflug A, Pitzer E, et al. Architecture and design of the heuristiclab optimization environment. In: Klempous R, Nikodem J, Jacak W, Chaczko Z, editors.

- Advanced Methods and Applications in Computational Intelligence. Heidelberg: Springer International Publishing. ISBN 978-3-319-01436-4; 2014, p. 197–261. doi:10.1007/978-3-319-01436-4_10.
- [65] Jofre L, del Rosario ZR, Iaccarino G. Data-driven dimensional analysis of heat transfer in irradiated particle-laden turbulent flow. *Int J Multiph Flow* 2020;125:103198. doi:10.1016/j.ijmultiphaseflow.2019.103198.
- [66] Ergun S. Fluid flow through packed columns. *Chem Eng Prog* 1952;48:89–94.
- [67] Wen CY, Yu YH. Mechanics of fluidization. *Chem Eng Prog Symp Ser* 1966;62:100–11.
- [68] Di Felice R. The voidage function for fluid-particle interaction systems. *Int J Multiph Flow* 1994;20(1):153–9. doi:10.1016/0301-9322(94)90011-6.
- [69] Garside J, Al-Dibouni MR. Velocity-voidage relationships for fluidization and sedimentation in solid–liquid systems. *Ind Eng Chem Process Des Dev* 1977;16(2):206–14. doi:10.1021/i260062a008.
- [70] Capecelatro J, Desjardins O, Fox RO. On fluid-particle dynamics in fully developed cluster-induced turbulence. *J Fluid Mech* 2015;780:578–635. doi:10.1017/jfm.2015.459.
- [71] Akiki G, Jackson TL, Balachandar S. Force variation within arrays of monodisperse spherical particles. *Phys Rev Fluids* 2016;1:044202. doi:10.1103/PhysRevFluids.1.044202.
- [72] Esteghamatian A, Euzenat F, Hammouti A, Lance M, Wachs A. A stochastic formulation for the drag force based on multiscale numerical simulation of fluidized beds. *Int J Multiph Flow* 2018;99:363–82. doi:10.1016/j.ijmultiphaseflow.2017.11.003.
- [73] Lattanzi AM, Tavanashad V, Subramaniam S, Capecelatro J. Stochastic models for capturing dispersion in particle-laden flows. *J Fluid Mech* 2020;903:A7. doi:10.1017/jfm.2020.625.

- [74] Akiki G, Jackson TL, Balachandar S. Pairwise interaction extended point-particle model for a random array of monodisperse spheres. *J Fluid Mech* 2017;813:882–928. doi:10.1017/jfm.2016.877.
- [75] Akiki G, Moore W, Balachandar S. Pairwise-interaction extended point-particle model for particle-laden flows. *J Comput Phys* 2017;351:329–57. doi:10.1016/j.jcp.2017.07.056.
- [76] Seyed-Ahmadi A, Wachs A. Microstructure-informed probability-driven point-particle model for hydrodynamic forces and torques in particle-laden flows. *J Fluid Mech* 2020;900:A21. doi:10.1017/jfm.2020.453.